Lab Notes

Editors
Thomas M. Moses | Shane F. McClure | Sally Eaton-Magaña

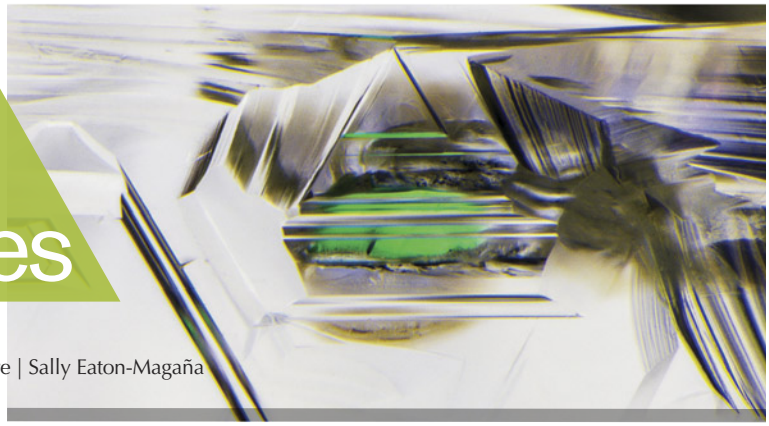

DIAMOND

Etch Features Reveal the Morphology of Diamond

Natural monocrystalline diamonds formed in the earth's mantle have two major growth forms: octahedron and cube. It has been suggested that diamond growth habit depends on multiple factors, including crystallization temperature, growth rate, and the degree of carbon supersaturation in the diamond-forming fluids (J.W. Harris et al., "Morphology of monocrystalline diamond and its inclusions," *Reviews in Mineralogy and Geochemistry*, Vol. 88, No. 1, 2022, pp. 119–166). If a diamond forms under changing conditions, it might not have a regular octahedral or cubic morphology but a combination of both. In some cases, diamonds grow without any well-defined crystal faces and are referred to as "irregular diamonds" (see examples in R. Tappert and M.C. Tappert, *Diamonds in Nature: A Guide to Rough Diamonds*, Springer-Verlag, Berlin, 2011, p. 28). While octahedral or cubic faces cannot always be identified visually in irregular diamonds, the morphology can be inferred by etch features left on the diamond by fluids in the mantle or during kimberlite eruption. Trigons and tetragons are the most common of these etch features—restricted to octahedral and cubic crystal faces, respectively.

Figure 1. Table (left) and pavilion (right) views of a chameleon diamond with visible trigons and tetragons. The trigons and tetragons are shown in more detail in figures 2 and 3. The diamond measures 1.28 cm in length.

The Carlsbad laboratory recently examined a 2.00 ct Fancy brown-greenish yellow diamond with both trigons and tetragons on its surface (figure 1). The trigons were located within a small indented natural near the table facet, while the tetragons were preserved within an indented natural at the culet (figures 2 and 3). Co-occurring trigons and tetragons are very uncommon and indicate an irregular morphology, characterized by both octahedral and cubic growth.

This stone was identified as a chameleon diamond. For such a classification, the diamond must include a green color component, show phosphorescence to short-wave UV, and change from a greenish color to a yellow or orange color with gentle heating or when kept in the dark for an extended period (C.M. Breeding et al., "Natural-color green diamonds: A beautiful conundrum," Spring 2018 *G&G*, pp. 2–27). These diamonds typically have a broad visible absorption band centered at approximately 480 nm and are referred to as "480 nm band diamonds." A study on rough yellow diamonds from Canada showed that all of those colored by the 480 nm absorption band have irregular morphology (M.Y. Lai et al., "Yellow diamonds with colourless cores – evidence for episodic diamond growth beneath Chidliak and the Ekati mine, Canada," *Mineralogy and Petrology*, Vol. 114, 2020, pp. 91–103), suggesting

Editors' note: All items were written by staff members of GIA laboratories.

Gems & Gemology, Vol. 59, No. 3, pp. 356–369.

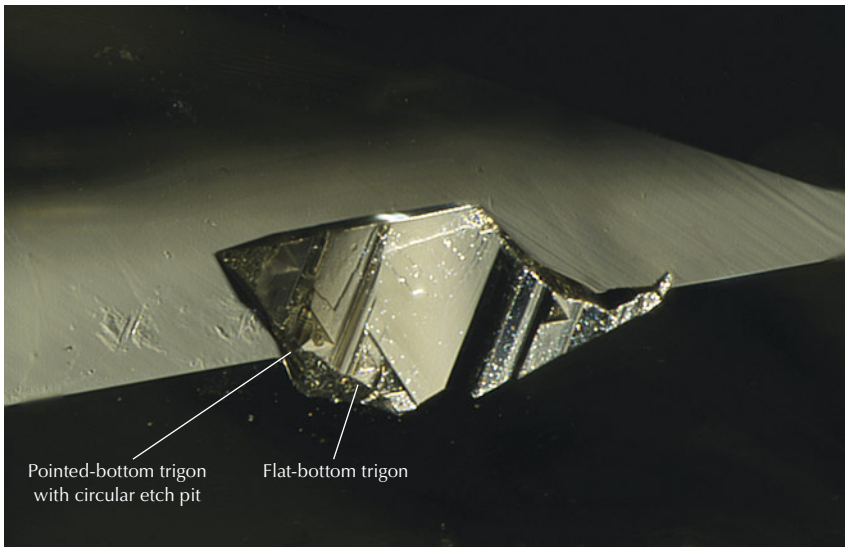

Figure 2. Flat-bottom and pointed-bottom trigons (surface features restricted to an octahedral crystal face) preserved on an unpolished portion of the diamond. A circular etch pit overprinting a pointed-bottom trigon indicates a late-stage diamond dissolution event that postdated the formation of the trigon. Field of view 1.26 mm.

that diamonds with the 480 nm absorption band may form under changing conditions in the mantle.

Trigons on diamond have two major morphologies: either a flat bottom or a pointed bottom (pyramidal). The type of trigon is primarily dependent on the temperature and pressure at the position where diamond dissolution occurs, as well as on the carbon dioxide and water contents in the fluid that etches diamonds. Experimental work indicates that fluids with higher carbon dioxide content tend to produce pointed-bottom rather than flat-bottom trigons (Y. Fedortchouk, "A new approach to understanding diamond surface features based on a review of experimental and natural diamond studies," *Earth-Science Reviews*, Vol. 193, 2019, pp. 45–65). Both forms of trigons were observed on the chameleon diamond we examined, as well as a circular etch pit overprinting a pointed-bottom trigon (figure 2). Unlike pointed-bottom trigons, circular pits are typically created by fluids with low carbon dioxide contents, indicating a late-stage etching event after the formation of the trigon.

The combination of surface features provides clues for the morphology of diamonds in rough form, as well as the interactions between diamonds and fluids throughout their journey from mantle residence to the earth's surface.

Mei Yan Lai and Matthew Hardman

Figure 3. Tetragons (surface features restricted to the cubic crystal face) preserved at the culet of the diamond. Field of view 1.26 mm.

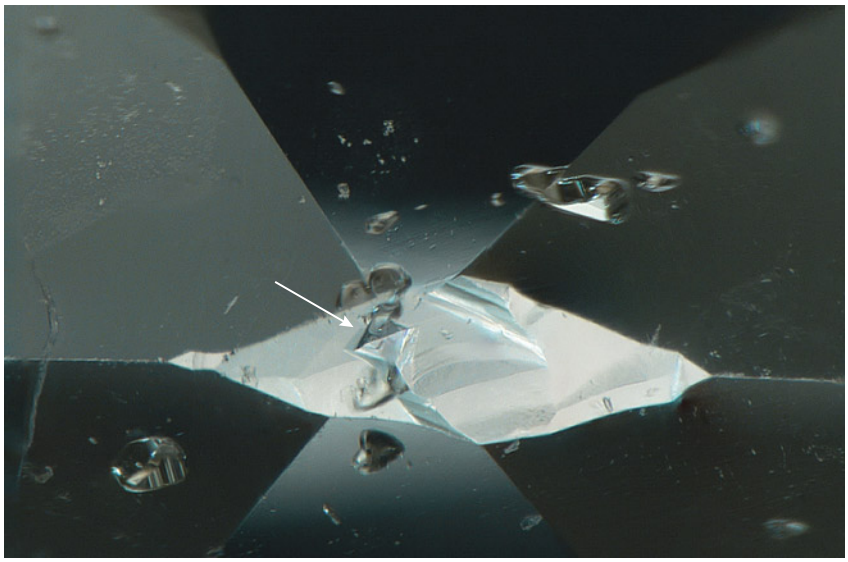

Natural Diamond with Unusual Phosphorescence

Phosphorescence spectroscopy shows that natural type IIb diamonds can have two broad phosphorescence bands: one centered at 500 nm that appears greenish blue and one centered at 660 nm that appears red. Generally, one of these phosphorescence bands is dominant. In the Hope diamond, for example, the phosphorescence initially appears orangy red and transitions to red as the subordinate greenish blue phosphorescence fades away (S. Eaton-Magaña et al., "Using phosphorescence as a fingerprint for the Hope and other blue diamonds," *Geology*, Vol. 36, No. 1, 2008, pp. 83–86). Occasionally, the faster-decaying greenish blue phosphorescence band will transition to the slower-decaying red band (Spring 2007 Lab Notes, pp. 47–48).

Recently, a 0.90 ct diamond with D color and I_1 clarity was submitted to GIA's laboratory in Ramat Gan, Israel, for a diamond dossier report. Infrared (IR) absorption spectroscopy indicated that the natural diamond was nominally type IIa. However, photoluminescence (PL) spectroscopy revealed that the diamond contained boron-related features, including the 648.2 nm peak attributed to a boron interstitial (B. Green, "Optical and

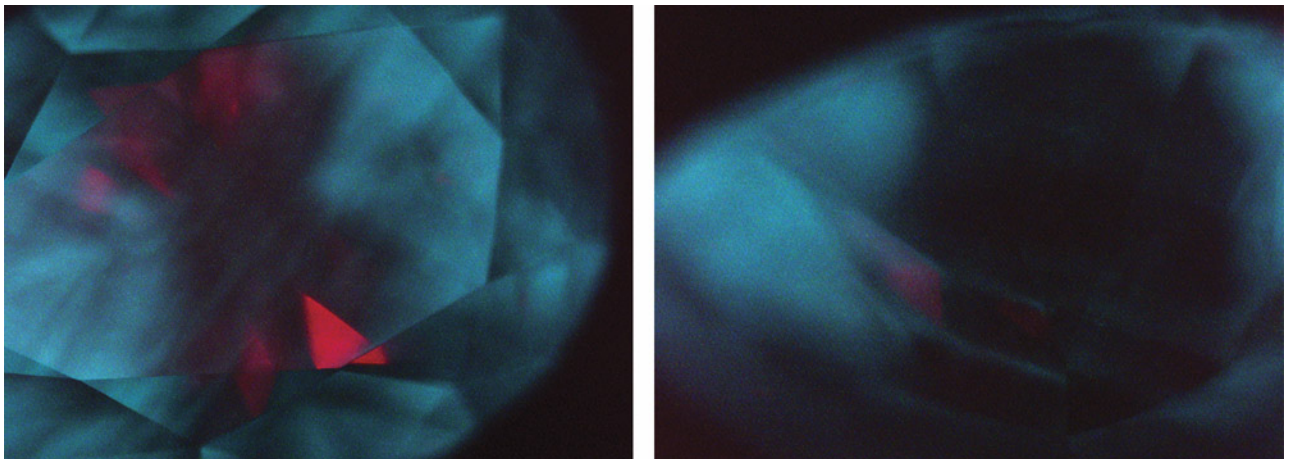

Figure 4. These deep-UV (<225 nm) phosphorescence images of the table (left) and pavilion (right) in a 0.90 ct D-color natural diamond with very low boron showed localized areas of the 500 nm (greenish blue) and 660 nm (red) bands.

magnetic resonance studies of point defects in single crystal diamond," PhD thesis, University of Warwick, 2013), along with the observed phosphorescence. These features indicated that the diamond did contain boron, but below the detection level of IR absorption spectroscopy. The distinctive aspect was that both the red and greenish blue phosphorescence were localized and visible within the same image (figure 4).

The phosphorescence is attributed to donor-acceptor pair recombination. For the 500 nm band, this recombination has been identified as interactions between boron acceptors and isolated nitrogen donors (J. Zhao, "Fluorescence, phosphorescence, thermoluminescence and charge transfer in synthetic diamond," PhD thesis, University of Warwick, 2022), while the 660 nm band is attributed to boron acceptors and unknown donors that are likely related to plastic deformation (S. Eaton-Magaña and R. Lu, "Phosphorescence in type IIb diamonds," *Diamond and Related Materials*, Vol. 20, No. 7, 2011, pp. 983–989). PL maps were collected on the table and pavilion with 455, 532, and 785 nm excitation; only an undefined PL feature at 813 nm showed an apparent increase on the pavilion within the red-phosphorescing region (figure 4, right).

Type IIb diamonds grown by high-pressure, high-temperature (HPHT) methods almost always show the 500 nm phosphorescence and occasionally a separate orange phosphorescence band centered at 580 nm. In a few instances, HPHT-grown diamonds have shown the 500 and 580 nm bands simultaneously in different portions of the diamond (Eaton-Magaña and Lu, 2011; Spring 2023 Gem News International, pp. 155–156).

This is the first time the authors have seen spatially distinct observations of red and greenish blue phosphorescence in a natural diamond, an unusual find.

Sally Eaton-Magaña, Evelina Goldort, and Dani Binyamin

Natural Type IIa Diamond with Unusual Red Fluorescence Distribution

The Carlsbad laboratory received a natural type IIa diamond with some unusual characteristics. As part of the standard data collection, the diamond type was determined by Fourier-transform infrared (FTIR) spectroscopy and deep-UV fluorescence images collected using the DiamondView instrument. The DiamondView images revealed predominantly red fluorescence on one side of the diamond and blue fluorescence on the other. This 3.58 ct pear modified brilliant diamond had H color and received an SI_2 clarity grade due to cavities, chips, and a feather (figure 5).

Type IIa diamonds typically display a blue fluorescence pattern under deep UV as a result of "band A" fluorescence or the N3 defect in the stone (U.F.S. D'Haenens-Johansson et al., "Synthesis of diamonds and their identification," *Reviews in Mineralogy and Geochemistry*, Vol. 88, No. 1, 2022, pp. 689–753). High amounts of nitrogen vacancy (NV) centers can cause red fluorescence in diamonds;

Figure 5. This 3.58 ct natural type IIa diamond with H color and SI_2 clarity displayed a unique fluorescence pattern when exposed to deep-UV light.

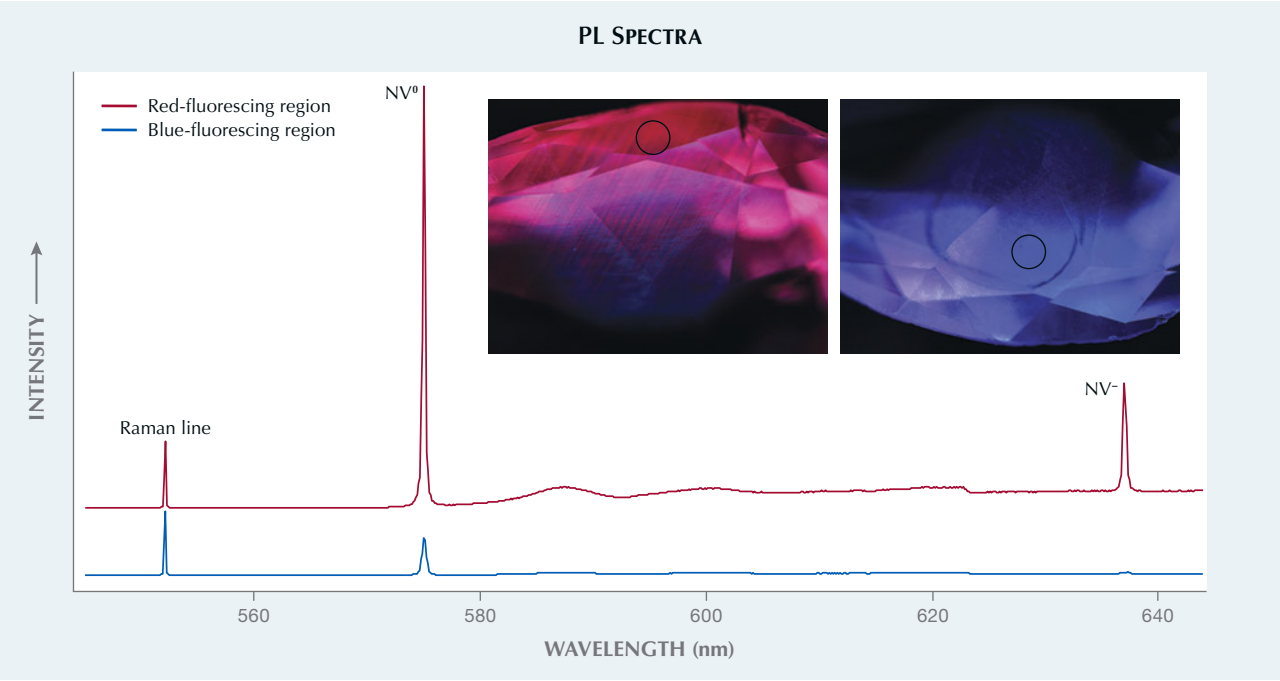

Figure 6. 514 nm PL spectra collected on the pavilion of opposite sides of the stone. The spectrum plotted in red corresponds with the red-fluorescing region, and the blue spectrum corresponds with the blue-fluorescing region, with Raman lines at 552 nm scaled as equal. Spectra are offset vertically for clarity. PL analysis spots are circled in the deep-UV fluorescence images.

however, this is rare in type IIa stones, as they are defined by nitrogen concentrations low enough to be undetectable by FTIR (Summer 2016 Lab Notes, pp. 189–190). The NV centers can be detected in a negative charge state (NV^-, zero-phonon line at 637 nm) or a neutral state (NV^0, zero-phonon line at 575 nm). Photoluminescence (PL) testing revealed much higher concentrations of both NV centers in the red-fluorescing region of the stone (figure 6). This distribution could have occurred if traces of isolated nitrogen were concentrated in one growth area of the stone.

PL mapping using 532 nm laser excitation (figure 7) displayed the relative intensities of these defects, demonstrating the wide distribution of the NV centers in opposite sides of the table and crown facets of this diamond. Analysis of this interesting fluorescence feature demonstrated that nitrogen could have been distributed unevenly in a relatively pure type IIa diamond when it initially formed.

Taryn Linzmeyer and Barbara Whalen

Figure 7. False-color 532 nm PL map showing the Raman-normalized peak area of NV^0 (left) and NV^- (right). The maps were compiled from 47,040 spectra. The pronounced gradient in NV centers across the diamond resulted in the different fluorescence color observations (see figure 6 insets).

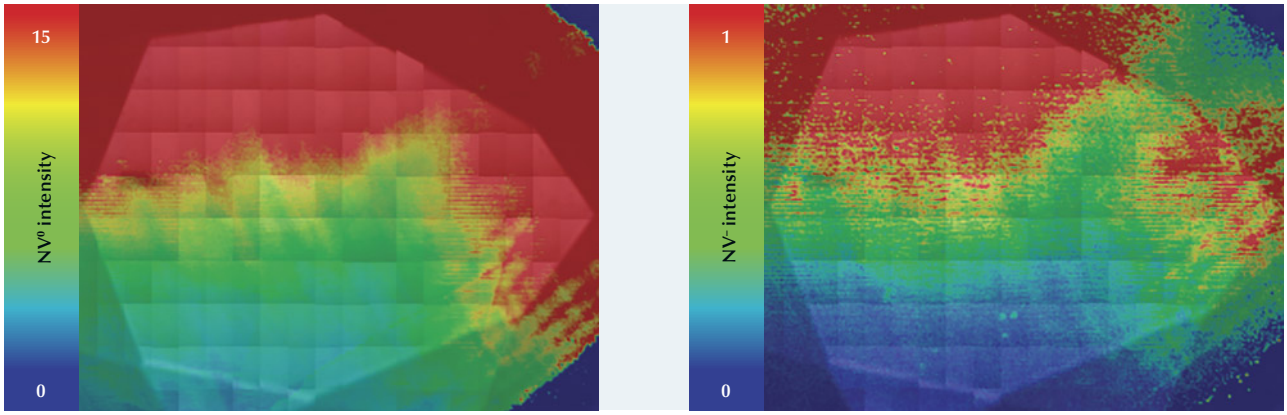

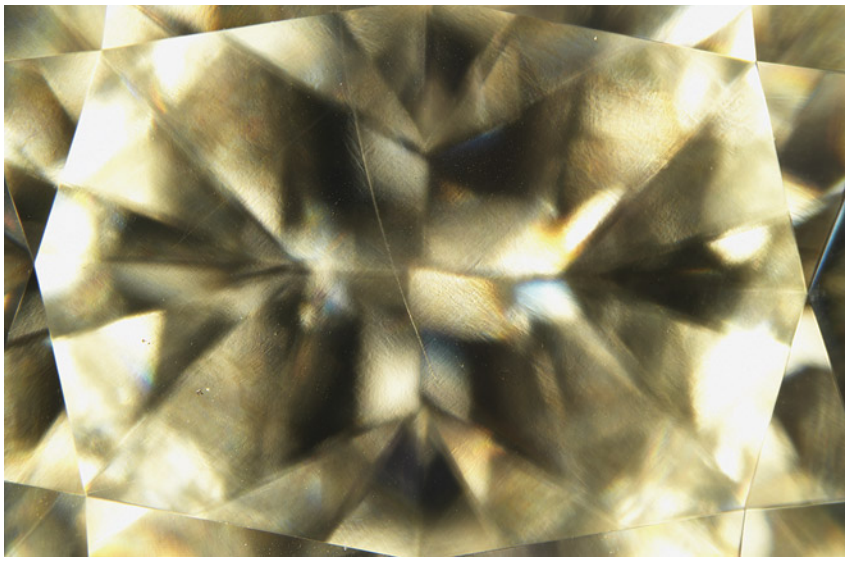

Figure 8. The etch channel in this CVD laboratory-grown diamond extends across the table facet into the crown. Field of view 7.19 mm.

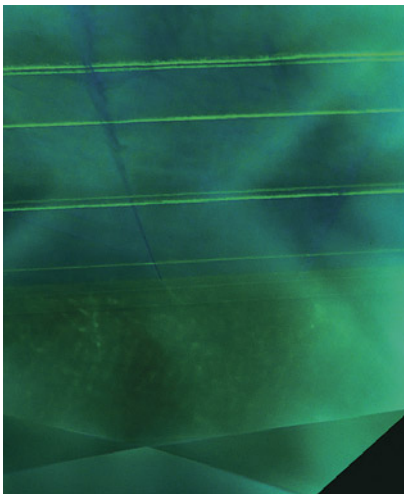

Figure 10. DiamondView imaging revealed that the channel was surrounded by blue-fluorescing dislocation bundles extending across the growth layers of the CVD diamond.

LABORATORY-GROWN DIAMOND

CVD "Etch" Channel

GIA's New York laboratory recently examined a diamond that had been grown via chemical vapor deposition (CVD) and processed using a high-pressure, high-temperature (HPHT) treatment. Standard grading procedures identified it as a 4.00 ct H-color cushion modified brilliant with SI_1 clarity. The diamond was identified as HPHT processed primarily due to the green fluorescence observed in the stone (see figure 10), while distinct fluorescent growth layers across the table and pavilion confirmed its CVD origin.

Figure 9. Dark residue is visible in some parts of the channel, as seen through the pavilion. The appearance of the residue is similar to that of graphitized carbon but could also be attributed to non-diamond carbon. Field of view 1.99 mm.

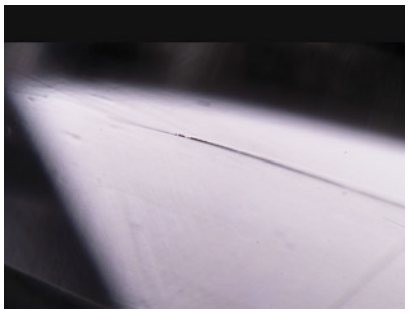

While GIA regularly receives CVD-grown diamonds submitted for laboratory-grown diamond reports, this particular example exhibited a unique characteristic. An etch channel–like structure was plainly visible across the table of the stone, a feature not observed in CVD laboratory-grown diamonds at GIA so far. The channel broke the surface of the table and extended across the stone, ending near a pavilion facet on the other side (figure 8). When viewed under high magnification, a dark residue (figure 9) was observed around parts of the channel. This residue was not present throughout the channel and appeared to be opaque. Close to the surface-reaching channel on the table facet were multiple smaller channels contained within the diamond. The surface-reaching opening of the channel was imaged with a scanning electron microscope (SEM), which revealed a jagged, slit-shaped entrance, suggesting that the shape of the channel extending throughout the diamond structure was similar in nature (figure 11). Some fragmentary material trapped just inside the entrance of the opening appeared to extend into the channel itself. This fragmentary material could have been the same type of opaque residue observed in some areas of the channel.

Fluorescence imaging with the DiamondView instrument also revealed the presence of this channel, which could be discerned by the blue-fluorescing line of dislocation bundles following the channel's path (figure 10). These dislocation bundles appeared almost perpendicular to the green-fluorescing growth layer boundaries, suggesting the channel was

Figure 11. A secondary electron SEM image showed the finer structure of the channel opening, revealing a jagged, slit-like feature. Field of view 16 µm.

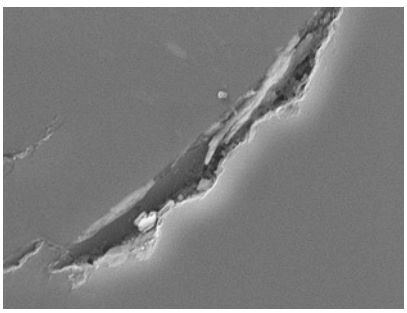

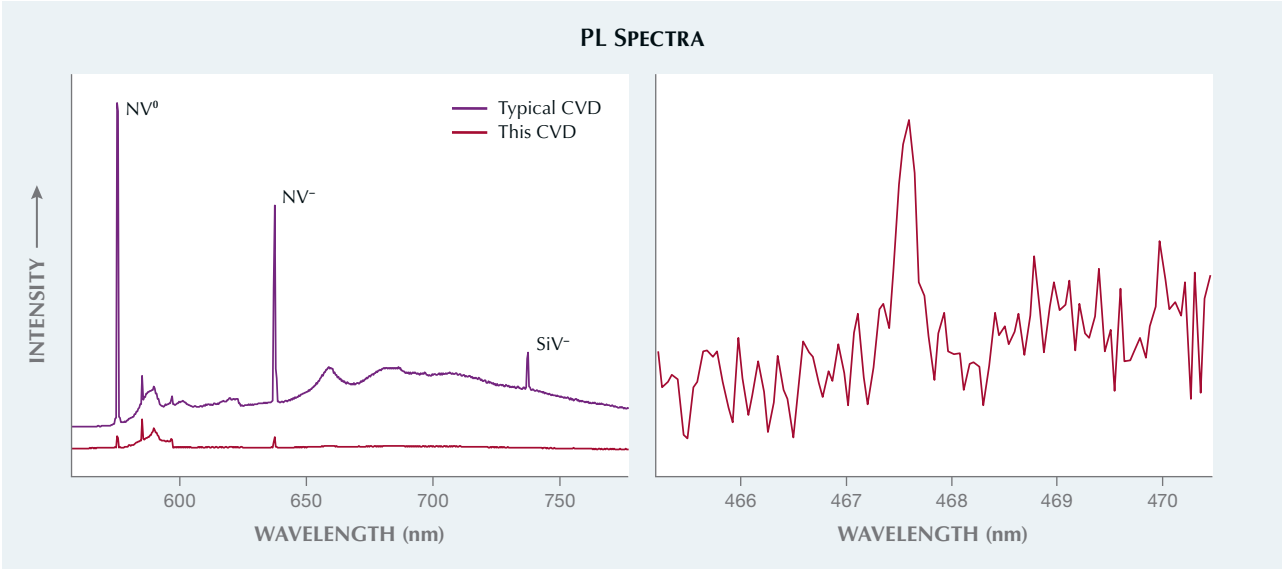

Figure 12. The PL spectra for a 1.40 ct CVD-grown diamond are shown in red. Left: The 514 nm PL spectrum reveals relatively weak NV centers and no detectable silicon. For comparison, the 514 nm PL spectrum for a more commonly observed as-grown CVD (purple) shows much stronger NV centers and detectable silicon. The Raman lines (not shown) are scaled as equal. Spectra are offset vertically for clarity. Right: Many locations on the CVD-grown diamond were analyzed with 457 and 633 nm excitation to verify whether the 468 nm center or the SiV^- center could be detected; this very weak peak of the 468 nm center was only detected at the culet.

created by exploiting weaker dislocation bundles that propagated through the diamond during CVD growth.

The presence of this channel in a CVD laboratory-grown diamond and the shape of the channel opening were unlike any natural etch channel opening or laser drill hole opening previously seen. It is unclear whether this channel was created during initial CVD growth or during HPHT processing. The opaque residue visible in some parts of the channel as well as the material visible at the channel surface could point to the presence of graphitized carbon, suggesting the channel was a byproduct of HPHT treatment, or it might indicate the presence of non-diamond carbon, which is a common feature found in untreated CVD laboratory-grown diamonds. In summary, the residue may arise from either the CVD growth process or post-growth treatment. Because this feature has not previously been documented at GIA, future studies may help determine the mechanism of action that could create channels in CVD-grown diamonds.

Elina Myagkaya

CVD-Grown Diamond with Few Diagnostic Features

Diamonds grown by chemical vapor deposition (CVD) have evolved rapidly in the last two decades. However, the vast majority submitted to GIA for reports still show several diagnostic features such as the silicon vacancy or SiV^- defect (a doublet at 736.6 and 736.9 nm) and/or the 468 nm peak when analyzed by photoluminescence (PL) spectroscopy. Additionally, most CVD diamonds have distinctive fluorescence images when analyzed by deep UV with the DiamondView instrument.

Therefore, it was interesting to analyze a 1.40 ct E-color, VVS_2 type IIa diamond submitted for a laboratory-grown diamond report. Initial PL data collection did not show either the SiV^- center or the 468 nm peak. The features observed were a 3H peak at 503.5 nm using 455 nm excitation and relatively weak nitrogen vacancy (NV) centers at 575 (NV^0) and 637 (NV^-) nm using 514 nm excitation (figure 12, left). The stone showed weak anomalous birefringence indicating strain; while this observation is helpful in confirming whether a diamond is grown by high-temperature, high-pressure (HPHT) methods, such birefringence cannot distinguish between natural and CVD origins. The deep-UV fluorescence image showed only deep blue coloration, which appeared generally comparable with the vast majority of natural type IIa diamonds (figure 13, left). Therefore, many of the standard markers of CVD origin were not present even when examined using advanced methods. Careful analysis of the fluorescence image revealed some distinct differences from the majority of natural diamonds, namely the patchiness of the fluorescence with some inert regions.

Many models of the DiamondView instrument include a series of filters that permit fluorescence imaging in which portions of the visible spectrum are blocked out. Using these filters, the blue portion of the visible spectrum was blocked in order to observe weaker underlying fluorescence features. With the orange long-pass filter blocking wavelengths less than 550 nm, NV-related fluorescence clearly showed the striations indicative of

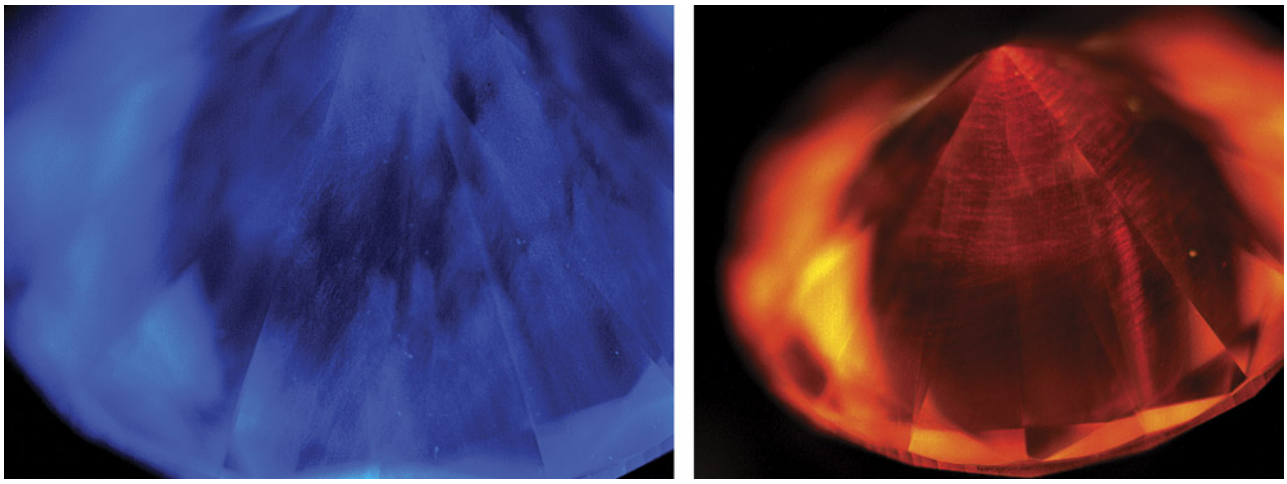

Figure 13. Left: The deep-UV (<230 nm) fluorescence image showed blue coloration (due to the presence of dislocation bundles) that appeared nominally similar to DiamondView images of natural type IIa diamonds. Right: When the fluorescence was filtered by an orange long-pass filter that blocked wavelengths below 550 nm, the NV-related fluorescence and the striations indicative of CVD growth became apparent.

CVD growth (figure 13, right). Also, several locations of the diamond were analyzed with PL spectroscopy to determine if either the 468 nm center or the SiV^- could be detected. Only at the culet was a small 468 nm feature observed (figure 12, right).

The author concluded that this was a CVD-grown diamond with no evidence of post-growth treatment. This example is a noteworthy indicator that as CVD growth methods improve, telltale defects are being minimized or eliminated entirely. Careful examination of all data, both spectroscopic and fluorescence imaging, is needed to provide accurate origins for diamond.

Sally Eaton-Magaña

Solid Laboratory-Grown Single-Crystal Diamond Ring

Carved single-crystal diamond rings are rare, with few examples to reference (see Spring 2020 Lab Notes, pp. 132–133). But with advancing technology in the laboratory-grown diamond industry, the creation of solid faceted diamond rings is now a reality. Recently submitted to the New York laboratory was a 4.04 ct single-crystal laboratory-grown diamond ring (figure 14). The 3.03 mm thick band had an inner diameter of 16.35–16.40 mm and an outer diameter of 20.32–20.40 mm. The ring was produced by Dutch Diamond Technologies in collaboration with the Belgian jewelry store Heursel, established in 1745.

This laboratory-grown diamond ring was cut from an 8.54 ct plate grown by chemical vapor deposition (CVD). Laser cutting produced a near-perfect circular ring, as demonstrated using digital imaging analysis to measure its inner and outer circumferences (figure 15).

The manufacture of a solid single-crystal diamond ring is a complex and challenging process. Once material is removed from the crystal, very fine fractures and imbalanced strain can have severe consequences, and the ring can shatter. Processing can take more

Figure 14. The 4.04 ct ring fashioned from a single-crystal CVD-grown diamond.

Figure 15. OpenCV software was used to draw perfect circles from the center of the ring, marked by a green dot.

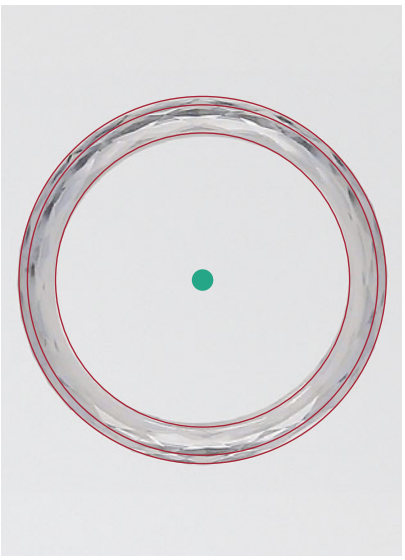

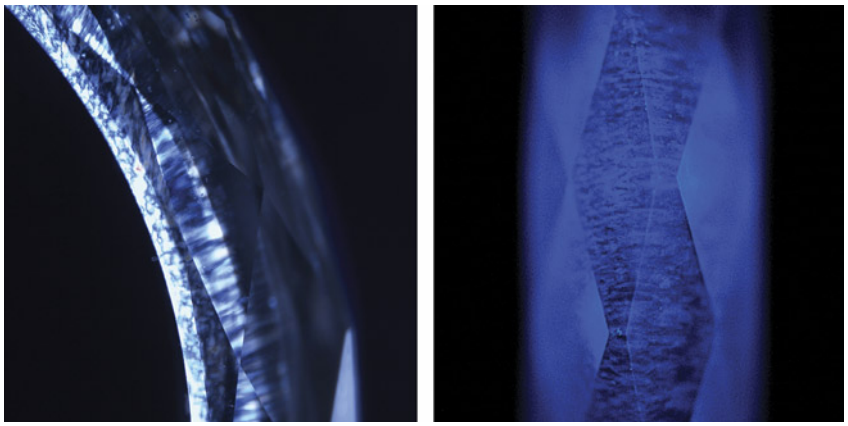

Figure 16. Strong birefringence observed under cross-polarized light (left) and blue fluorescence observed in the DiamondView (right).

than six months. Creating the ring from a single-crystal laboratory-grown diamond involved about 1,131 hours of processing (including pre-grinding) in the Dutch town of Cuijk, followed by 751 hours of polishing in Belgium.

Infrared absorption analysis revealed it was a type IIa diamond (no detectable nitrogen), and no hydrogen-related peaks were detected at 3107 or 3123 cm^{-1}. Photoluminescence spectroscopy showed interesting vacancy-related defects indicative of a multi-step growth process. A very strong emission from the silicon vacancy (SiV^-) defect was observed with 633 nm laser excitation; this is a common feature used to identify CVD-grown diamond. The conclusion was that this ring had not undergone post-growth treatment; nevertheless, it was notable that the ring showed relatively low nitrogen-related defects such as NV centers, along with no detectable 468 nm peak or the 596/597 nm doublet. P. Martineau et al. ("Identification of synthetic diamond grown using chemical vapor deposition (CVD)," Spring 2004 *G&G*, pp. 2–25) observed the 596/597 doublet with a 514 nm laser. Also of note, there were no H3 or 468 nm centers detected with 457 nm laser excitation.

Strong birefringence was observed using cross-polarized light under microscopic analysis, with an unusual radial pattern (figure 16, left) signifying unique growth conditions compared to typical CVD diamonds available in the market today. The deep ultraviolet illumination of the DiamondView (figure 16, right) confirmed these unusual growth features with a lack of post-growth fluorescence colors such as green produced by the H3 center.

The solid laboratory-grown diamond ring was studied by GIA and determined to have VVS_2 clarity based on dark non-diamond carbon pinpoint inclusions (growth remnants typical of CVD-grown diamonds) with Good polish (polishing on the interior surface of the ring precluded Very Good). Although the ring was a near-perfect circle (figure 15), symmetry was considered not applicable. The diamond had an E color specification based on GIA's color grading scale. The ring was laser inscribed "Laboratory-Grown" on a side facet.

The quality and size of this solid diamond ring (see the video clip at www.gia.edu/gems-gemology/fall-2023-lab-notes-solid-CVD-ring) provide a great example of the advancing technology in laboratory-grown diamonds and changing trends in the jewelry industry. This is the first time a GIA laboratory has examined a colorless diamond ring fashioned entirely from a laboratory-grown diamond.

Paul Johnson, Stephanie Persaud, and Madelyn Dragone

PEARLS

A Traditional Bombay Pearl Bunch

During the era when the maharajahs and maharanis ruled much of India, natural pearls were in great demand. In the nineteenth and early twentieth centuries, many merchants from the Middle East relocated to Bombay (now Mumbai) to benefit from this demand (R. Carter, *Sea of Pearls*, Arabian Publishing, London, 2012, pp. 169–175). Thus, it is no surprise that India has been a significant center of pearl manufacturing, processing, and trading for centuries. To showcase their high-quality pearls, traders and artisans in Bombay would sort the pearls, string them with silk threads, and tie them together at both ends using decorative metallic cords of various colors. These bunches were in great demand in the heyday of the natural pearl market and were sold as "Bombay bunches" (M. Manutchehr-Danai, *Dictionary of Gems and Gemology*, Springer, Berlin and Heidelberg, 2008, p. 101).

Recently, GIA's Mumbai laboratory had the opportunity to examine an 80-year-old Bombay bunch inherited by one of the city's established pearl families. The bunch consisted of 553 light cream round and near-round drilled pearls, strung in nine hanks, each containing four strands, with the exception of one hank with seven strands. The hanks were tied at both ends with white metal wires, together with silver and blue cords and tassels (figure 17). The pearls ranged from 3.83 to 5.72 mm, and the total weight of the bunch was approximately 80.51 g. The owner stated that the total weight of the pearls was approximately 130 chow (equivalent to 331.8 ct or 66.35 g). Chow is a system of converting weight into volume (*The Pearl Blue Book*, CIBJO, 2020).

The strung pearls were perfectly matched in color and exhibited smooth surfaces with high luster. When viewed under 40× magnification, they all exhibited typical nacreous overlapping aragonite platelets. Their internal structures were examined by real-time microradiogra-

Figure 17. A Bombay bunch consisting of nine hanks and 553 high-quality natural pearls ranging from 3.83 to 5.72 mm.

phy. The majority revealed fine growth arcs and concentric ringed structures, while others revealed tight or minimal structures, some with small faint cores or light organic-rich cores (figure 18). It was evident that these were natural pearls from *Pinctada*-species mollusks, as their internal structures were very similar to those observed in *Pinctada radiata* pearls from the Arabian (Persian) Gulf when compared to GIA's research database.

All pearls showed an inert reaction when exposed to optical X-ray fluorescence analysis. Energy-dispersive X-ray fluorescence spectrometry on a few samples revealed manganese values ranging from below detection limits to 30.7 ppm and strontium values of 1215 to 1989 ppm, consistent with a saltwater growth environment. Raman analysis using 514 nm excitation was also carried out on the surface of selected pearls showing a doublet at 702/705 cm^{-1} as well as a peak at 1085 cm^{-1}, indicative of aragonite. Very weak polyenic pigment-related peaks at 1130 and 1530 cm^{-1} were also observed in a few of the pearls, likely associated with their light cream coloration (A. Al-Alawi et al., "Saltwater cultured pearls from *Pinctada radiata* in Abu Dhabi (United Arab Emirates)," *Journal of Gemmology*, Vol. 37, No. 2, 2020, pp. 164–179). The photoluminescence spectra under 514 nm excitation were also consistent with the Raman results and displayed high fluorescence together with the aragonite peaks, typical of most nacreous pearls. When exposed to long-wave ultraviolet light, the pearls showed a moderate blue reaction.

Figure 18. Real-time microradiography images of eight pearls from the Bombay bunch revealing fine growth arcs and concentric ringed structures typical of those internal structures observed in Pinctada radiata *pearls.*

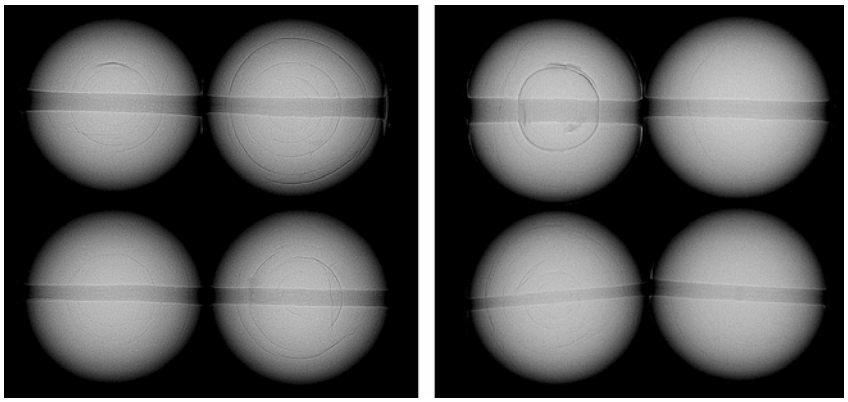

Historically, Bombay bunches were known to contain high-quality *Pinctada radiata* pearls fished from the Arabian (Persian) Gulf, commonly referred to as "Basra pearls" in the trade. Records indicate that the proportion of round pearls found in each natural pearl harvest today is less than 5% (H. Bari and D. Lam, *Pearls*, Skira, Milan, 2010, p. 43). Natural pearls are rare to find, and it can take decades to match a round pair of similar size, color, and luster. Encountering Bombay bunches in today's

Figure 19. A white button-shaped atypical bead cultured pearl weighing 8.15 ct and measuring 11.73 × 11.35 × 9.03 mm.

market is a rarity, and it was a great opportunity for GIA Mumbai to examine such an interesting and memorable pearl submission.

Pfokreni Nipuni, Abeer Al-Alawi, and Roxane Bhot Jain

Flame-Like Surface Structure in a Nacreous Atypical Bead Cultured Pearl

GIA's Mumbai laboratory recently received an atypical bead cultured pearl with a unique surface appearance. The white button-shaped pearl weighed 8.15 ct and measured 11.73 × 11.35 × 9.03 mm (figure 19).

Viewed under 40× magnification, the surface exhibited typical fine nacreous overlapping aragonite platelets, but a distinct pattern similar to the flame structures observed in some porcelaneous pearls was also noted (Summer 2021 Lab Notes, pp. 152–153). These flame-like features were formed due to the presence of relatively opaque, frosty white rounded depressions on the pearl's surface. Although rounded, they seemed to be oriented longitudinally and were more tapered toward the base and apex and broader along the sides of the pearl (figure 20). Also observed on the surface were small white spots with slightly elongated comet tails that flowed tangentially to the circumference of the button. The base and apex of the pearl lacked the whitish subsurface opaque features that produced the flame structure effect, and these two areas appeared more translucent than the other parts of the pearl.

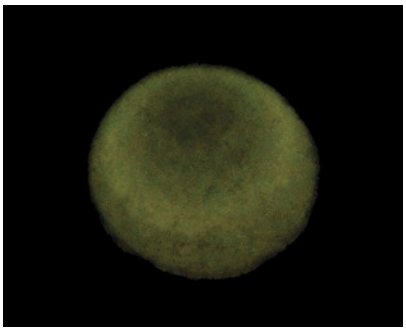

Figure 21. XRF reaction of the pearl, with the sides appearing brighter than the base and apex.

Under long-wave ultraviolet radiation, the pearl showed a strong yellowish green reaction, and a similar but weaker reaction was noted under short-wave ultraviolet radiation. The deep-UV (<230 nm) radiation of the DiamondView instrument revealed a clear bluish reaction, with the surface showing a chalky white flame-like structure extending from the apex center across the pearl. Raman analysis of the pearl's surface using a 514 nm excitation showed a doublet at 701/704 cm^{-1} as well as peaks at 1086 and 1464 cm^{-1} characteristic of aragonite. The photoluminescence spectra revealed high fluorescence, with a maximum centered at approximately 620 nm.

Energy-dispersive X-ray fluorescence spectrometry revealed a low manganese level of 16.9 ppm and a higher strontium level of 1577 ppm, indicative of a saltwater environment. However, when exposed to X-ray fluorescence (XRF) analysis, the pearl exhibited a moderate yellowish green fluorescence with a higher intensity toward the sides but a weaker reaction on the base and apex (figure 21). Saltwater pearls are usually inert when tested by this method, while freshwater pearls and saltwater bead cultured pearls with freshwater shell nuclei tend to fluoresce weak to strong yellowish green. In the case of bead cultured pearls, a thinner nacre usually produces a stronger reaction; conversely, the thicker the nacre, the weaker the reaction.

Real-time microradiography imaging (RTX) revealed a long, complex linear feature in the center typically associated with non-bead cultured pearls (figure 22, left). When viewed under X-ray computed microtomo-

Figure 20. Rounded depressions forming the flame-like structure. Field of view 0.4 mm.

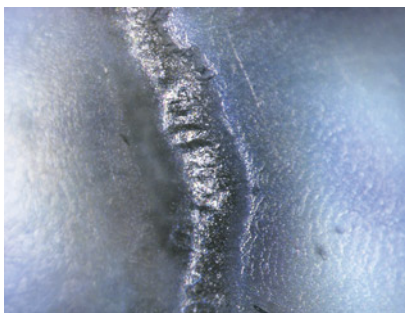

Figure 22. Left: RTX image of the pearl's internal structure with a large linear feature. Right: μ-CT image showing a freshwater-type linear feature in the center and a faint boundary (arrow).

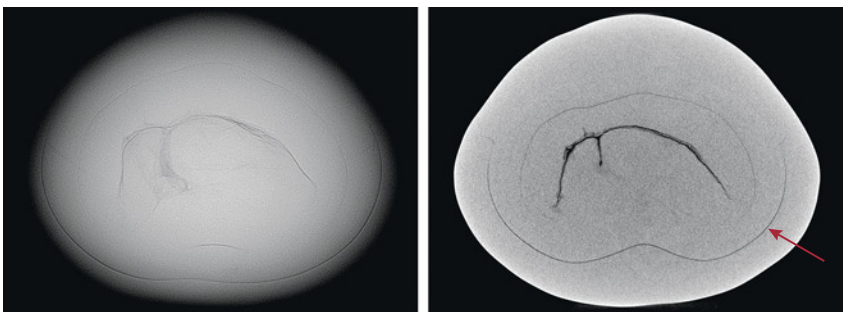

graphy (μ-CT), the linear feature looked very similar to those often observed in freshwater non-bead cultured pearls. A faint boundary was also seen around the central linear feature (figure 22, right) and other growth rings. All these observations, together with the XRF reaction of the pearl and the saltwater chemistry, were indicative of an atypical bead cultured saltwater pearl with a freshwater pearl used as its nucleus (P. Kessrapong and K. Lawanwong, "Atypical bead cultured *Pinctada maxima* pearls nucleated with freshwater non-bead cultured pearls," *GIA Research News*, April 6, 2020). The nacre thickness overlying the freshwater non-bead cultured pearl nucleus ranged from approximately 1.09 to 1.90 mm. The thicker nacre was positioned near the base and apex and the thinner nacre toward the sides. This aligned with the XRF reaction observed, as a thinner saltwater nacre will allow more fluorescence from the freshwater pearl nucleus to pass through the nacre layers, while thicker nacre masks the reaction.

Over the years, GIA has encountered similar atypical bead cultured pearls with sizeable freshwater non-bead cultured pearls used as a nucleus (Spring 2023 Lab Notes, pp. 74–76). However, the presence of flame-like structures seen on nacreous pearls is a very rare phenomenon. This combination of interesting culturing along with the unique surface features make this pearl noteworthy.

Prasad Mane, Nishka Vaz, and Abeer Al-Alawi

*Figure 23. Two traditional Indian-style pearl nose rings (*nath*) set with colored gemstones and pearls measuring approximately 6.63 × 6.09 mm to 8.42 mm (left) and 5.38 mm to 8.02 × 7.61 mm (right).*

Pearls in Traditional Indian Nose Rings

The beauty of Indian jewelry lies in the artisanship involved in creating intricate, unique designs. One example is the classic Indian nose ring (known as the *nath*). It is typically cashew shaped, with a chain to connect it to a hairpiece or earring. The nath exemplifies traditional Maharashtrian jewelry and is usually crafted in yellow gold. Made famous during the Peshwa rule, the nath has been crafted using diamonds, pearls, rubies, and emeralds. Today, the nath is worn mainly for weddings or special occasions, while everyday nose adornments take the form of smaller, simpler studs or rings made from gold or silver. Recently, GIA's Mumbai laboratory received two traditional nose rings for pearl identification.

Each was set with 17 drilled pearls, near-drop and button, ranging from light cream to cream in color. They were skillfully strung together with yellow metal wire and set with colored gemstones of various shapes and cutting styles. The pearls in the larger nose ring (figure 23, left) ranged from approximately 6.63 × 6.09 mm to 8.42 mm, and the item weighed a total of 13.96 g. Those in the smaller nose ring (figure 23, right) ranged from 5.38 mm to 8.02 × 7.61 mm, and this piece weighed 9.05 g overall. When viewed under 40× magnification, the pearl surfaces in both pieces showed typical nacreous overlapping aragonite platelets and a medium to high surface luster. Energy-dispersive X-ray fluorescence (EDXRF) spectrometry revealed manganese levels below the instrument's detection level and a strontium content averaging 950 ppm. In addition, the pearls were inert to X-ray fluorescence, indicative of saltwater origin. They showed a moderate greenish yellow reaction under long-wave ultraviolet light and a weaker reaction of similar color under short-wave UV. Real-time microradiography imaging revealed internal structures similar to those observed in natural pearl studies for various *Pinctada*-species mollusks (K. Scarratt et al., "Natural pearls from Australian *Pinctada maxima*," Winter

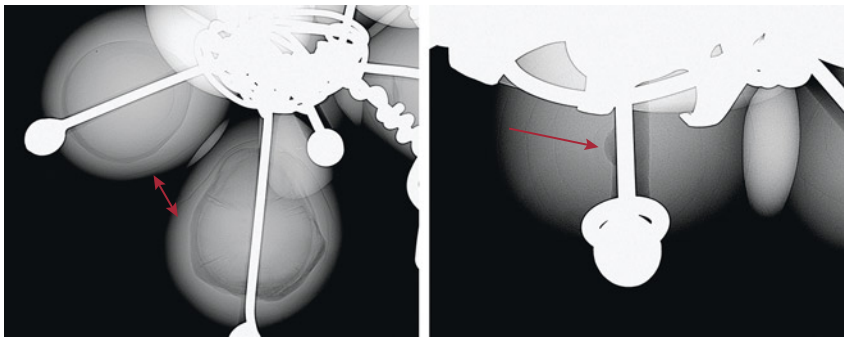

Figure 24. Real-time microradiography of the internal structures observed in the larger nose ring consisting of organic-rich acicular structures and growth arcs (left) and a "collapsed core" near the drill hole area surrounded by growth arcs (right).

2012 *G&G*, pp. 236–261; N. Nilpetploy et al., "The gemological characteristics of Pipi pearls reportedly from *Pinctada maculata*," Winter 2018 *G&G*, pp. 418–427). The radiopaque areas visible on the microradiographs of both items correspond to the yellow metal fittings and wire, since they are denser and prevent X-rays from passing through.

Five pearls from the larger nath revealed an organic-rich internal structure with varying patchy light and dark gray contrasting areas, along with an acicular structure radiating from their centers that occupied almost half of the internal structure (figure 24, left). Two pearls showed "collapsed cores" close to the drill holes (figure 24, right); the bulk of the cores, if any, were removed as a result of drilling. The remaining ten pearls displayed fine concentric rings and growth arcs, all proving their natural origin.

Microradiography of the pearls in the smaller nath revealed similar internal structures. While the majority of those pearls showed fine concentric rings and growth arcs, three of them (marked with arrows in figure 25) also possessed organic-rich and acicular cores that occupied varying degrees of their structure. The internal structures observed in both items contained classic natural pearl structures similar to those observed in known *Pinctada radiata* pearls in GIA's research database. The EDXRF results were also within the range expected for *Pinctada radiata* samples, with the lower levels of strontium (average of 950 ppm) and manganese (mostly below detection limits) consistent with that mollusk species and below those expected from *P. maxima* pearls (A. Homkrajae et al., "Internal structures of known *Pinctada maxima* pearls: Natural pearls from wild marine mollusks," Spring 2021 *G&G*, pp. 2–21).

The combinations of natural pearls made these two pieces very attractive. It is no easy task to create traditional nose ornaments with pearls of such size. These two unique pearl jewelry items provide an excellent example of Indian heritage.

Lubna Sahani, Abeer Al-Alawi, and Roxane Bhot Jain

Figure 25. The majority of the pearls in the smaller nose ring showed faint growth arcs and concentric ringed structures, while three of them showed organic-rich acicular cores (marked with arrows) typical of natural pearls.

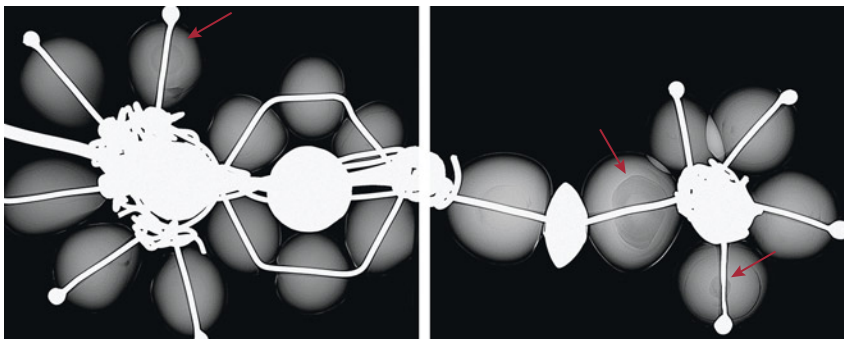

RUBY

"Nebula" Inclusion in Ruby Beryllium-Diffused to Heal Fractures

Recently the Carlsbad laboratory received a 4.12 ct purple-red stone measuring approximately 11.50 × 7.70 × 4.72 mm (figure 26) for identification services. It featured unusual veil-like reddish color zoning wafting throughout a purple bodycolor. The refractive index measured 1.760–1.770, identifying the stone as a ruby.

Figure 26. An unusual ruby with coloring reminiscent of a nebula found in the depths of outer space.

Figure 27. Fingerprints resulting from flux-assisted heating of a beryllium-rich flux. Field of view 7.19 mm.

Microscopic examination indicated that the reddish color zoning was associated with altered fingerprints that resembled a cosmic nebula due to a flux-rich residue (figure 27). These fingerprints appeared to be consistent with fractures that had been healed using a flux-assisted heating process in a high-heat environment.

Due to the indications of high heat, laser ablation–inductively coupled plasma–mass spectrometry (LA-ICP-MS) chemical analysis was performed to check for the presence of beryllium diffusion. Initially, LA-ICP-MS conducted on two spots revealed beryllium concentrations of <0.019 ppma and 60.87 ppma. This significant discrepancy prompted additional LA-ICP-MS testing in three spots, revealing beryllium concentrations of <0.19 ppma, 1780 ppma, and <0.19 ppma. Microscopic observation of the testing spots showed areas of high beryllium on or near the reddish color zones, while areas of very low beryllium were associated with testing areas on the purple areas of the stone.

Therefore, it was concluded that a beryllium-rich flux was used to heal the fractures naturally present in the stone. The ruby was likely heated in this flux at temperatures high enough to allow the beryllium to seep from the flux into the stone, but not long enough for the beryllium to infiltrate its entirety.

Michaela Damba

Translucent Ruby Filled with Zinc Glass

Recently the Carlsbad laboratory received an 8.57 ct translucent purplish red heart-shaped mixed-cut stone for identification service (figure 28). Standard gemological testing revealed a refractive index of 1.760–1.769, and a ruby spectrum was obtained with a handheld spectroscope. The stone showed a medium to strong red fluorescence to long-wave UV radiation and a very weak red fluorescence to short-wave UV radiation. During microscopic analysis, several fractures containing a whitish filler and air pockets were seen using fiber-optic lighting (figure 29). Using reflected light, fractures with a lower luster than the host corundum were also observed, which confirmed the presence of a filling material.

The stone did not show the blue flash effect typically observed in rubies filled with lead glass (S.F. McClure et al., "Identification and durability of lead glass–filled rubies," Spring 2006 *G&G*, pp. 22–36). Although the filler improved the durability, it did not appear to improve the clarity.

Glass filling treatment has been used on heavily fractured rubies to increase their clarity and durability since the early 1980s, and cavity filling was noted and described as early as 1984. The original filler was silica glass, which was easily visible since its refractive index (~1.5) is significantly lower than corundum (R.E.

Figure 28. An 8.57 ct heart-shaped fracture-filled ruby treated with a zinc glass filling.

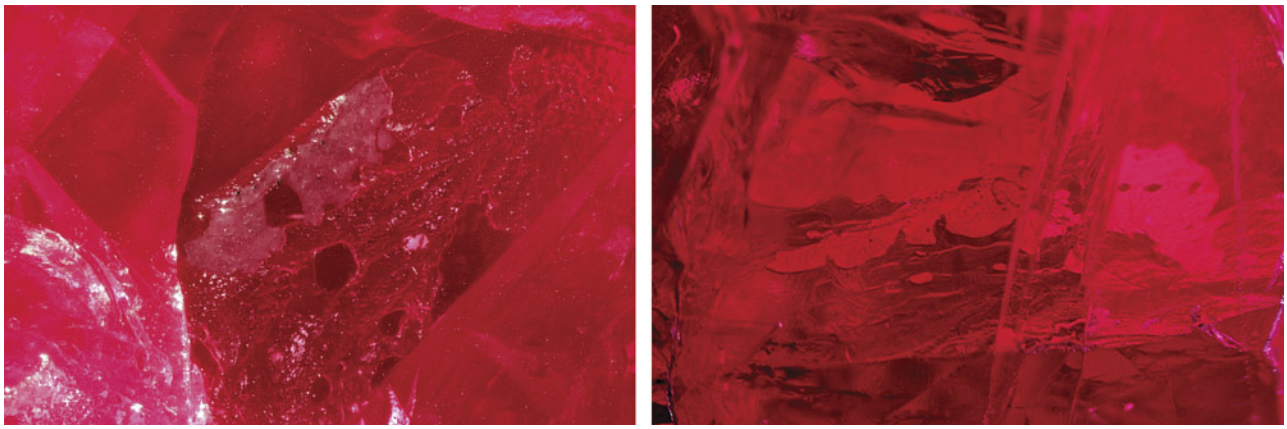

Figure 29. A fracture with whitish filler (left) and trapped air pockets (right). Fields of view 1.58 mm (left) and 2.90 mm (right).

Kane, "Natural rubies with glass-filled cavities," Winter 1984 *G&G*, pp. 187–199). In early 2004, gemologists discovered a new type of glass filler with high lead content and a much better clarity enhancement due to its higher reflective index (~1.70) (GAAJ Research Laboratory, "Lead-glass impregnated ruby," March 15, 2004). Since then, lead glass fillers have become the most popular filler for rubies, although other glass types such as bismuth and cobalt have also been used (T. Leelawatanasuk et al., "Cobalt-doped glass-filled sapphire: An update," *Australian Gemmologist*, Vol. 25, No. 1, 2013, pp. 14–20; Spring 2020 Lab Notes, p. 139).

In the heart-shaped ruby submitted to the laboratory, energy-dispersive X-ray fluorescence spectroscopy did not detect lead or bismuth but did show chromium, iron, and zinc. Additional chemical analysis was performed with laser ablation–inductively coupled plasma–mass spectrometry on two spots of one larger fracture with a substantial amount of filler in order to quantitatively measure the elements in the glass filler. The averages of the two analysis spots were 28750 ppmw silicon, 1091 ppmw zinc, and 108 ppmw lead.

Chemical results and gemological properties revealed that this glass filler was not the lead or bismuth glass the authors first suspected, but rather a silica-based glass doped with zinc. While this type of filler had visual properties similar to those of other glass fillers in corundum, it did not show a flash effect. This is the first time the authors have encountered a ruby filled with zinc glass.

Shiva Sohrabi and Amy Cooper

PHOTO CREDITS
Adriana Robinson—1, 26, 28; Matthew Hardman—2, 3; Evelina Goldort—4; Diego Sanchez—5; Barbara Whalen—6; Elina Myagkaya—8–10; Sally Eaton-Magaña—13 (right); Towfiq Ahmed—14, 15; Paul Johnson—16 (left); Madelyn Dragone—16 (right); Gaurav Bera—17, 19, 23; Nishka Vaz—20; Nathan Renfro—27; Shiva Sohrabi—29